Dealloying Synthesis of Bimetallic (Au−Pd)/CeO$_2$ Catalysts for CO Oxidation

Haiyang Wang,[‡] Dongxia Zhang,[‡] Ruiyin Zhang, Hao Ma, Huimin Zhang, Ruijuan Yao, Miaomiao Liang, Yuzhen Zhao, and Zongcheng Miao*

Cite This: *ACS Omega* 2023, 8, 11889−11896

Read Online

ACCESS | Metrics & More | Article Recommendations | Supporting Information

ABSTRACT: The nanorod-structured (Au−Pd)/CeO$_2$ catalysts with different Au/Pd ratios were prepared from Al−Ce−Au−Pd precursor alloys through combined dealloying and calcination treatment. XRD, SEM, TEM, XPS, Raman spectroscopy, and N$_2$ adsorption−desorption measurements were applied to test the structure and physicochemical properties of samples. Catalytic evaluation results imply that the (Pd$_{0.15}$−Au$_{0.15}$)/CeO$_2$ catalyst calcined at 500 °C possesses optimal catalytic activity for CO oxidation when compared with other catalysts with different Au/ Pd ratios or (Pd$_{0.15}$-Au$_{0.15}$)/CeO$_2$ calcined at other temperatures, whose 50% and 99% reaction temperature can be reached as low as 50 and 85 °C, respectively. This superior catalytic property is attributed to their robust nanorod structure and the introduction of noble bimetal Pd and Au, which can construct a nanoscale interface to access fast electron motion, thus enhancing catalytic efficiency.
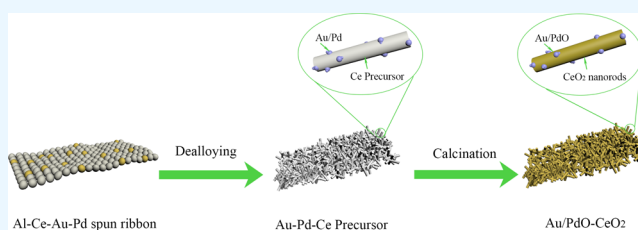
INTRODUCTION

The catalytic CO oxidation reaction is of great practical significance for CO pollution control in daily life and industrial production.[1−4] Extensive research on CO oxidation has been conducted by using noble metals like Pt,[5] Pd,[6] Au,[7] and Rh[8] to explore the influence of the structure and interface effect on catalytic activity.[9−11] Pt-group metals are the earliest proposed type of catalysts because of their high activity for CO oxidation.[12−14] The Au nanoparticles are reported to show superior catalytic activity for low-temperature CO oxidation when the particle size is smaller than 5 nm.[15,16] Typically, the bimetallic catalysts exhibit better properties when compared with the constituent individual metals due to the optimized geometric and electronic properties of active sites caused by the synergistic effects in bimetallic catalysts.[17−20] The catalytic performance of supported Au−Pd bimetallic catalysts has been investigated. Garcia's group researched the dynamic structure of Pd-doped Au$_{25}$ nanoclusters upon pretreatment and catalytic reaction.[21] They concluded that the fabricated PdAu$_{24}$ nanoclusters supported on titania showed significantly higher activity than supported monometallic Au$_{25}$ nanoclusters. However, the reported fabrication methods so far are relatively complicated and difficult for large-scale production.

CeO$_2$ is a unique rare metal oxide with rich reservation. It has attracted wide interest as a catalyst for CO oxidation due to its fast storing/releasing oxygen capability through a reversible Ce^{3+}/Ce^{4+} redox reaction.[22−24] The merits of low energy for oxygen vacancy formation and outstanding thermal stability also make CeO$_2$ a competitive material for catalytic field

application.[25−27] As the catalytic properties of materials can also be influenced by surface structure, CeO$_2$-based catalysts with various morphologies and facets like nanorod,[28] nanotube,[29] octahedron,[30] and nanoflower[31] have been reported. However, pure CeO$_2$ possesses poor catalytic properties because of the deficiency of highly active sites, which makes it hard for an adsorption/conversion reaction to take place. Supporting noble metals onto CeO$_2$ can efficiently support active sites and enhance the catalytic performance of the material;[32−34] CeO$_2$ with a large surface area can also promote dispersion of noble metals.[35] Chen's group synthesized bimetallic Au−Ag-deposited CeO$_2$ catalysts by a deposition−precipitation method. The Au− Ag/CeO$_2$ shows high CO conversion because of the formation of a bimetallic alloy with good dispersion.[36]

Dealloying is a simple, efficient, and environmentally friendly technique to fabricate nanoporous materials on a large scale.[37−39] The pore size and surface structure of materials can be controlled by regulating the corrosion temperature, reaction rate, and composition of alloys.[40,41] Transition metal oxides (NiO,[42] CuO,[43] Co$_3$O$_4$[44]) and noble metals (Ag,[45] Rh,[46,47] Pt[48]) have been reported to support the CeO$_2$ nanorod successfully.[49] The obtained CeO$_2$-based catalysts display
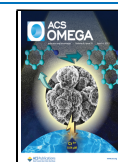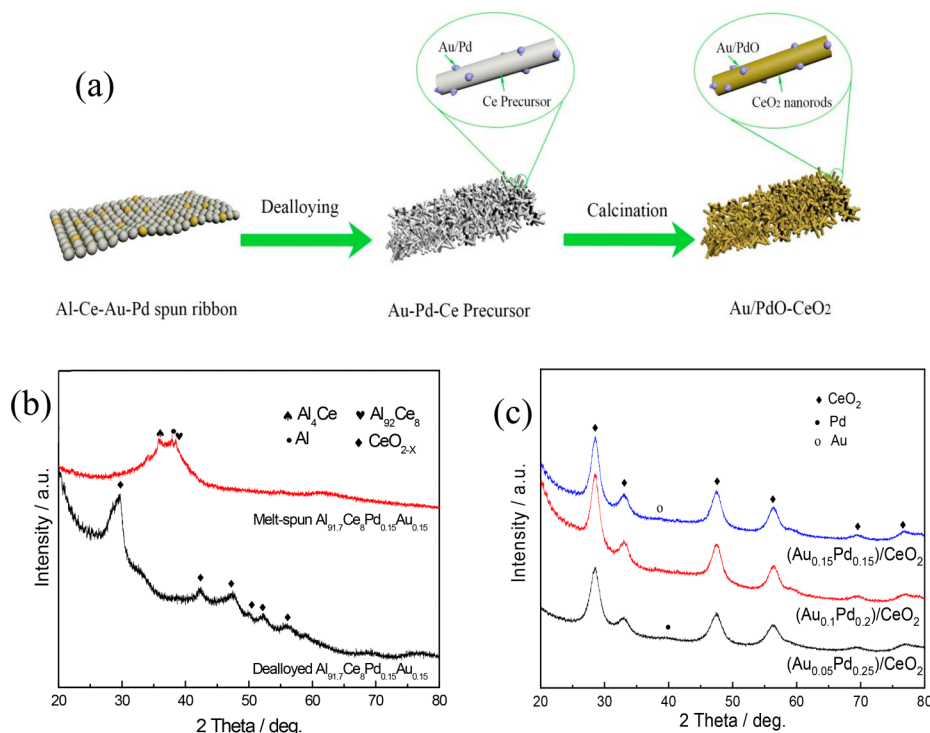
Figure 1. (a) Fabrication schematic of $(Pt-Au)/CeO_2$, XRD patterns of (b) melt-spun and dealloyed $Al_{91.7}Ce_8Au_{0.15}Pd_{0.15}$ ribbons, and (c) $(Au_X-Pd_{0.3-X})/CeO_2$ (X = 0.05, 0.1, 0.15) calcined at 500 °C.

outstanding catalytic activity. However, the research on noble bimetal supporting onto CeO_2 by dealloying method needs further exploration.

In this work, the catalytic activity of CeO_2-based nanocomposites is enhanced by adding noble bimetal Au and Pd into the system through a facile dealloying and calcination method. Almost all of the Al in the sample is etched and removed during the dealloying procedure and does not recover thereafter. The introduction of noble bimetal into CeO_2 can contribute to the formation of a nanoscale interface between Au (PdO) and CeO_2 nanorods, which can promote the move of electrons at the interface. The catalytic properties of samples with various Pd/Ag ratios and different heat treatment conditions are also evaluated. The results indicate that the $(Pd_{0.15}-Au_{0.15})/CeO_2$ exhibits the best catalytic performance with 50% reaction completion temperatures as low as 50 and 85 °C, respectively. This work provides a novel method for design and fabrication of high-efficient catalysts.

■ RESULTS AND DISCUSSION

In this work, the nanorod-shaped bimetal/CeO_2 framework catalyst is fabricated by a combined dealloying and calcination method, and the corresponding fabrication schematic is displayed in Figure 1a. The XRD patterns of melt-spun and dealloyed $Al_{91.7}Ce_8Au_{0.15}Pd_{0.15}$ ribbons are analyzed by using JADE software, with the results displayed in Figure 1b. The melt-spun Al–Ce–Au–Pd alloy ribbons are composed of α-Al, Al_4Ce, and $Al_{92}Ce_8$ phases. After dealloying treatment, the α-Al, Al_4Ce, and $Al_{92}Ce_8$ phases disappear while CeO_x, a new phase, is detected, indicating that most of the Al has been eliminated. The XRD patterns of dealloyed $Al_{91.7}Ce_8Au_{0.05}Pd_{0.25}$, $Al_{91.7}Ce_8Au_{0.1}Pd_{0.2}$, and $Al_{91.7}Ce_8Au_{0.15}Pd_{0.15}$ ribbons dealloyed at 500 °C are shown in Figure 1c. The diffraction peaks located at 28.4°, 33°, 47.4°, 56.4°, 69.4°, and 76.9° correspond to (111),

(200), (220), (311), (400), and (331) planes of cubic CeO_2 (PDF no. 89-8436), respectively, implying that the CeO_{2-x} phase has been totally transformed into the CeO_2 phase. The weak peaks at 38° and 40° are assigned to the (111) planes of Au and Pd, respectively. The EDS spectrum in Figure S1 illustrates that the atomic composition of Ce, Au, and Pd in $(Au_{0.15}-Pd_{0.15})/CeO_2$ catalyst is 95.81, 1.83, and 2.36 atom %, respectively, indicating that Au and Pd have been added into the Al–Ce precursor alloys successfully. More accurate elemental composition and noble metal mass loading of noble metals are tested by employing ICP, with the results shown in Table S1. The results show that the atomic ratios of Pd and Au in catalysts are close to those of the added noble metals.

The surface and cross-sectional images of $(Au-Pd)/CeO_2$ composites are presented in Figure 2. The composites are obtained by adding Pd and Au with a total amount of 0.3% (atom %) into the $Al_{92}Ce_8$ alloy. All three $(Au-Pd)/CeO_2$ samples exhibit a nanorod-supported framework structure with nanopores distributed among them. The structures of the samples remain similar without significant changes as the Au/Pd ratio varies, while the arrangement of pores is slightly tuned, as shown in Figure 2a–c. In addition, the cross-sectional SEM image of $(Au_{0.15}-Pd_{0.15})/CeO_2$ in Figure 2d further reflects the presence of rich pores and independent arrangement of nanorods. It is believed that the distinctive framework structure can contribute to the stabilization of samples during the catalytic process; the existence of pores distributed among nanorods can provide more channels for penetration of reacted gases, and thus, the catalytic CO oxidation performance is expected to be enhanced.

The more detailed microstructures of fabricated catalysts are characterized by TEM and HRTEM. As observed from the TEM images of $(Au_{0.05}-Pd_{0.25})/CeO_2$ (Figure 3a), $(Au_{0.1}-Pd_{0.2})/CeO_2$ (Figure 3c), and $(Au_{0.15}-Pd_{0.15})/CeO_2$ (Figure 3e), the
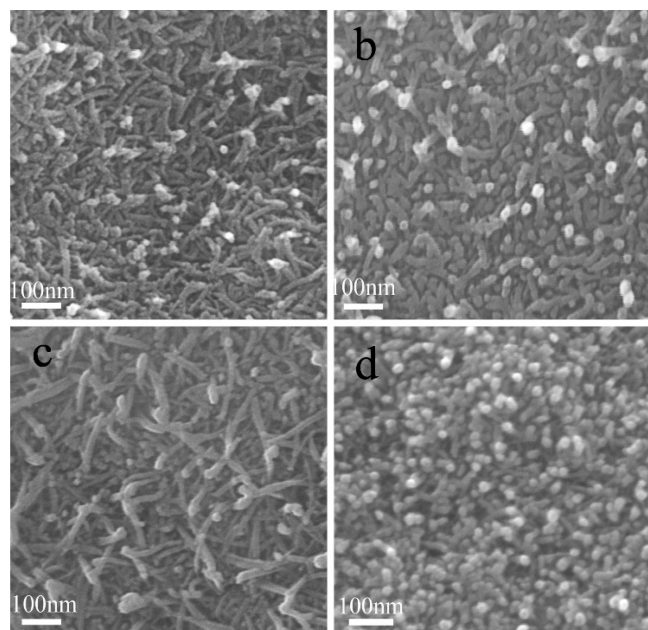
Figure 2. SEM images of (a) $(Au_{0.05}-Pd_{0.25})/CeO_2$, (b) $(Au_{0.1}-Pd_{0.2})/CeO_2$, (c) $(Au_{0.15}-Pd_{0.15})/CeO_2$, and (d) the cross-sectional image of $(Au_{0.15}-Pd_{0.15})/CeO_2$.
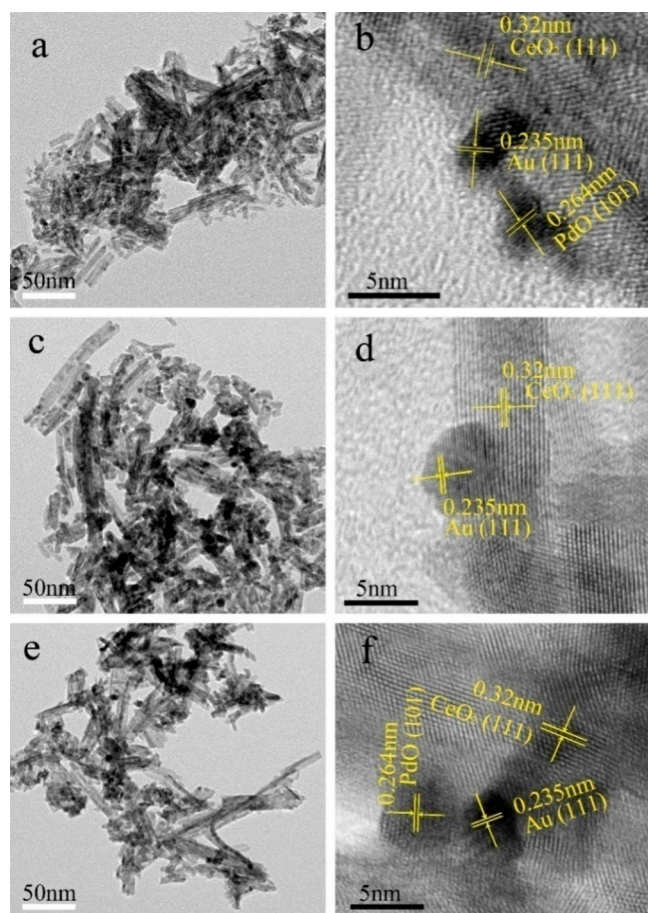
Figure 3. TEM and HRTEM images of (a, b) $(Au_{0.05}-Pd_{0.25})/CeO_2$, (c, d) $(Au_{0.1}-Pd_{0.2})/CeO_2$, (e, f) $(Au_{0.15}-Pd_{0.15})/CeO_2$.

$(Au-Pd)/CeO_2$ catalysts are composed of evenly arranged nanorods. The nanorods are interpenetrated and stack onto each

other; some black nanoparticles with average diameters of 5 nm are distributed on the surface of nanorods. These results are in line with SEM results. The corresponding HRTEM images are displayed in Figure 3b,d,f, respectively. The lattice fringe with a space of 0.32 nm corresponds to the (111) plane of CeO_2; the black nanoparticles with a lattice space of 0.235 nm correspond to the (111) plane of Au, while the lattice space of 0.264 nm belongs to the (101) plane of PdO. This further implies that Au and Pd have been added into the Al−Ce alloy system successfully. The surface element distribution state of Au and PdO on CeO_2 nanorods is further characterized by STEM mapping (Figure S2). For $(Au_{0.15}-Pd_{0.15})/CeO_2$ prepared through dealloying and calcination at 500 °C, the Pt and Au nanoparticles are semiembedded onto the surface of $(Au_{0.15}-Pd_{0.15})/CeO_2$, as shown in Figure S2.

The specific surface area, pore volume, and distribution of $(Au-Pd)/CeO_2$ catalysts are investigated by a N_2 adsorption−desorption test. As observed from the N_2 adsorption−desorption isotherms of three $(Au-Pd)/CeO_2$ samples in Figure 4a, the three curves are of type IV and possess an H3 hysteresis loop at a relative pressure of 0.75−1.0 P/P_0, which implies the existence of mesopores.[50] The BET specific surface area of $(Au_{0.05}-Pd_{0.25})/CeO_2$, $(Au_{0.1}-Pd_{0.2})/CeO_2$, and $(Au_{0.15}-Pd_{0.15})/CeO_2$ is 76.0114, 80.5366, and 89.5943 m^2 g^{-1}, respectively; their corresponding pore size distribution is centered around 19.51, 16.39, and 15.81 nm, and the pore volume is 0.37, 0.33, and 0.35 cm^3 g^{-1}, respectively, as shown from the BHJ pore-size distribution plots in Figure 4b. Therefore, it can be clearly observed that the $(Au_{0.15}-Pd_{0.15})/CeO_2$ composite material possesses the largest specific surface area and smallest pore volume.[51] Compared with Pt/CeO_2, the overall specific surface area of $(Au-Pd)/CeO_2$ is relatively low, which may be due to the coarsening phenomenon of partial nanorods during heat treatment at relatively high temperature, but the mesoporous properties of composites remain unchanged. Large specific surface area, proper pore size, as well as pore volume of $(Au_{0.15}-Pd_{0.15})/CeO_2$ can provide more gas diffusion paths and richer reactive sites, thus contributing to enhanced catalytic activity.[46]

The XPS characterization of $(Pd_{0.15}-Au_{0.15})/CeO_2$ catalyst is employed to measure chemical valence, with results as presented in Figure 5. Figure 5a−d displays the typical fitted Ce 3d, Pd 4f, Au 4f, and O 1s of $(Pd_{0.15}-Au_{0.15})/CeO_2$ obtained using the Gaussian fitting method. For the Ce 3d spectrum in Figure 5a, the binding energies located at 881.9, 888.2, and 897.7 eV for Ce $3d_{5/2}$ and 900.4, 907.3, and 916.2 eV for Ce $3d_{3/2}$ correspond to Ce^{4+}, and the peaks at 884.5 and 903.3 eV are assigned to Ce^{3+}.[52] As the concentration of Ce^{3+} can be reflected from the integrated areas of the Ce^{3+} peak to the total $(Ce^{3+} + Ce^{4+})$ peaks, the surface concentration of Ce^{3+} on the $(Pd_{0.15}-Au_{0.15})/CeO_2$ catalyst is 18.01% according to the fitting calculation of Ce 3d spectrum. The Pd 4f spectrum in Figure 5b demonstrates that both metallic Pd and ionic Pd^{2+} exist in $(Pd_{0.15}-Au_{0.15})/CeO_2$. The peaks at 336.2 and 341.2 eV correspond to the Pd $3d_{5/2}$ of Pd^0; the binding energies at 337.2 and 342.5 eV for Pd $3d_{5/2}$ and 342.5 eV for Pd $3d_{5/2}$ belong to Pd^{2+}.[33] Similarly, the Pd^{2+} concentration of total Pd is 27% and the ratio between Pd^0 and Pd^{2+} is around 7:3. For the Au 4f spectrum in Figure 5c, the binding energies at 83.6 eV for Au $4f_{7/2}$ and 87.2 eV for $4f_{5/2}$ are characteristic peaks of Au^0,[53] while the peaks at 84.6 and 88.1 eV are assigned to Au^{3+}. The O 1s spectrum is shown in Figure 5d, in which the peaks centered at ∼529.3, ∼531, and ∼532.2 eV correspond to lattice oxygen species (O_{lat}), surface adsorbed
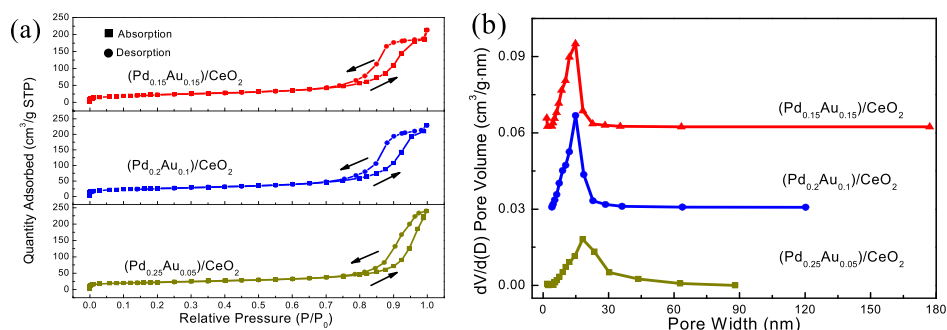
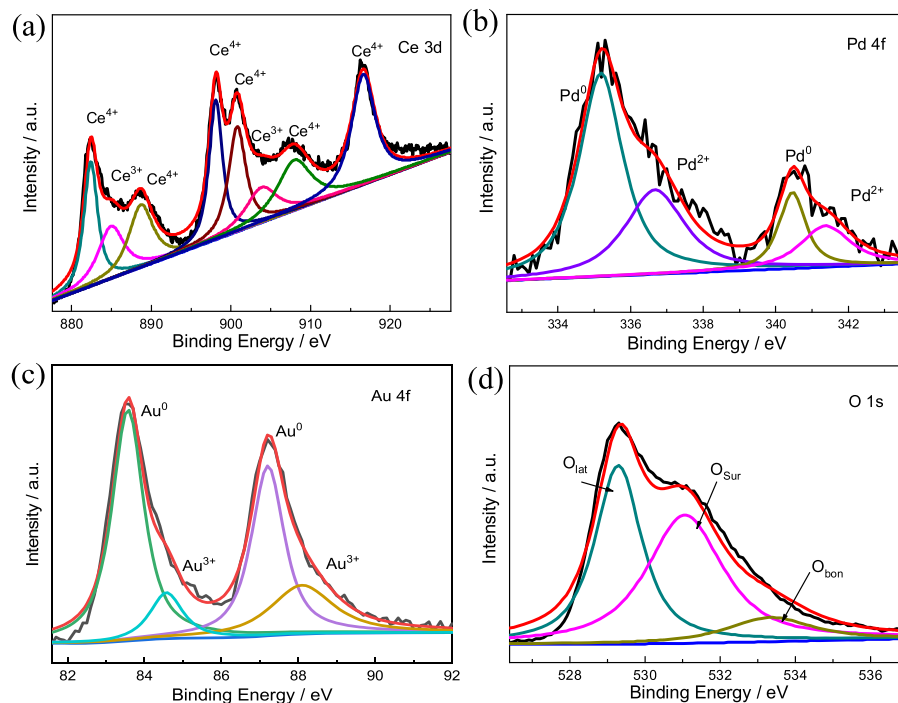**Figure 4.** (a) Nitrogen adsorption−desorption isotherms and (b) the BHJ pore size distribution of (Au−Pd)/CeO$_2$.

Figure 5. XPS spectra of (a) Ce 3d, (b) Pd 4f, (c) Au 4f, (d) O 1s of the (Pd$_{0.15}$-Au$_{0.15}$)/CeO$_2$ catalyst.

oxygen (O$_{sur}$), and weakly bonded specific oxygen species (O$_{bon}$), respectively. The concentration of surface-active oxygen for total oxygen in (Pd$_{0.15}$−Au$_{0.15}$)/CeO$_2$ is 20.8%. Therefore, highly concentrated Ce^{3+}, Au^0, and PdO species exist in the (Pd$_{0.15}$−Au$_{0.15}$)/CeO$_2$ catalyst. The presence of noble metal active phases is conducive to adsorbing CO onto the surface of catalyst; highly concentrated Ce^{3+} can provide more oxygen vacancies, which is conducive to generating more active oxygen atoms.

More molecular structural information on (Pd−Au)/CeO$_2$ catalysts is measured by Raman characterization. For the Raman spectra of three (Pd−Au)/CeO$_2$ catalysts with different Pd/Au ratios in Figure 6, the occurrence of an apparent peak around 456 cm^{-1} is attributed to the F$_{2g}$ vibrational mode of CeO$_2$ originating from the breathing mode of oxygen anions around Ce cations. Compared with the curve of pure CeO$_2$ in Figure S3, the peak intensity is obviously decreased, and the peak position is shifted from 459 to 456 cm^{-1}, which is ascribed to a common size-dependent phenomenon occurring in CeO$_2$-based particles and demonstrates the generation of large amount of grain boundaries/defects brought from grain refinement after introduction of Pd and Au nanoparticles into the material system.[46]
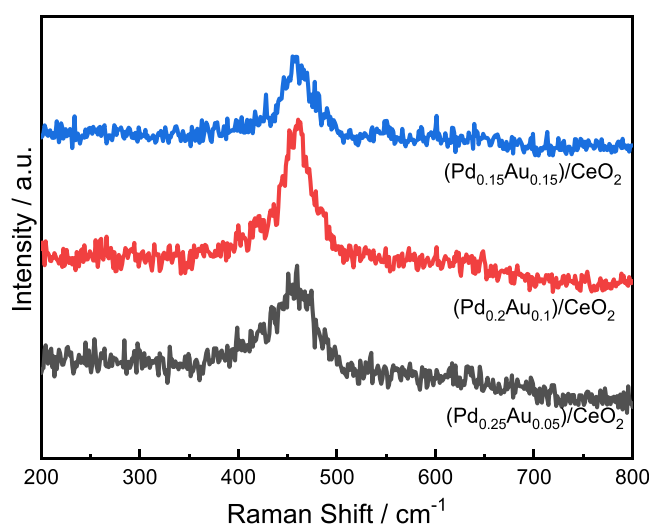

Figure 6. Raman spectra of (Pd−Au)/CeO$_2$ catalysts.

Figure 7a displays the relationship between the CO conversion rate and calcination temperature over (Au$_X$−
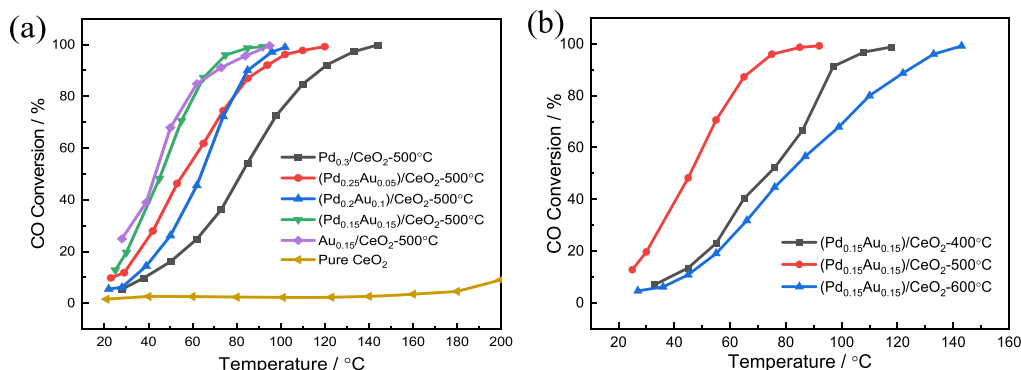
Figure 7. (a) CO conversion as a function of reaction temperature over the $(Pd-Au)/CeO_2$ catalysts; (b) $(Pd_{0.15}-Au_{0.15})/CeO_2$ catalyst prepared under different calcination temperatures.

$Pd_{0.3-X})/CeO_2$ (X = 0, 0.05, 0.1, 0.15, 0.3) catalysts. For $Pd_{0.3}/CeO_2$ with no addition of Au, the temperatures for 50% CO conversion (T_{50}) and 99% CO conversion (T_{99}) are 85 and 145 °C, respectively, which is much better than pure CeO_2 calcined at 300 °C (T_{50} = 235 °C, T_{99} = 320 °C, Figure S4). After introducing 0.05 atom % Au into the Al−Ce−Pd alloy precursor to partially substitute the Pd atom, a $(Pd_{0.25}-Au_{0.05})/CeO_2$ catalyst can be obtained that exhibits improved catalytic property with T_{50} and T_{99} decreased to 58 and 123 °C, respectively. Upon further increasing the atomic percentage of Au to 0.1 atom %, the catalytic temperature is reduced (T_{50} = 63 °C, T_{99} = 105 °C). The catalytic performance of the catalyst is optimal when Pd/Au = 0.15:0.15 and the corresponding T_{50} and T_{99} are as low as 50 and 85 °C, respectively. The total CO conversion temperature for the $(Pd_{0.15}-Au_{0.15})/CeO_2$ catalyst is better than that of the $Au_{0.15}/CeO_2$ catalyst (T_{99} = 95 °C). Therefore, the in situ loading of Pd and Au bimetallic metals onto CeO_2 can enhance the catalytic performance by playing the synergistic effect between two noble metal active phases; thus, a highly efficient catalyst at low cost can be realized. The influence of calcination temperature on CO conversion rate is also discussed and displayed in Figure 7b. The total CO conversion temperatures of $(Pd_{0.15}-Au_{0.15})/CeO_2$ at calcination temperatures of 400, 500, and 600 °C are 120, 80, and 143 °C, respectively. Obviously, the catalytic activity is improved as the calcination temperature increases from room temperature to 300 °C; which is reduced as the calcination temperature further increases. The catalytic activity of $(Pd_{0.15}-Au_{0.15})/CeO_2$ achieves a premium at an annealing temperature of 500 °C. Such performance is higher or competitive when compared with other CeO_2-based catalysts in Table S2.[29,44,54−56]

The long-term stability of the $(Pd_{0.15}-Au_{0.15})/CeO_2$ catalyst is evaluated to investigate its practical application potential, with the results displayed in Figure 8. At a catalytic temperature of 90 °C, the catalytic CO ability of the sample remains stable without decay after successive reactions under a mixed atmosphere of 1% CO, 10% O_2, and 89% N_2 for 70 h; when the catalytic temperature is decreased to 60 °C, a 58% CO conversion rate can be obtained after a successive 60 h reaction, implying the superior catalytic stability of the $(Pd_{0.15}-Au_{0.15})/CeO_2$ catalyst. The XRD pattern of $(Pd_{0.15}-Au_{0.15})/CeO_2$ catalyst after successive 60 h reaction at 60 °C in Figure S5 also shows that the sample structure is not changed significantly, further implying the structural stability of the catalysts.

A possible catalytic mechanism is proposed as follows. The porous structured $(Pd-Au)/CeO_2$ exhibits exceptional catalytic performance due to its distinctive porous structure and phase
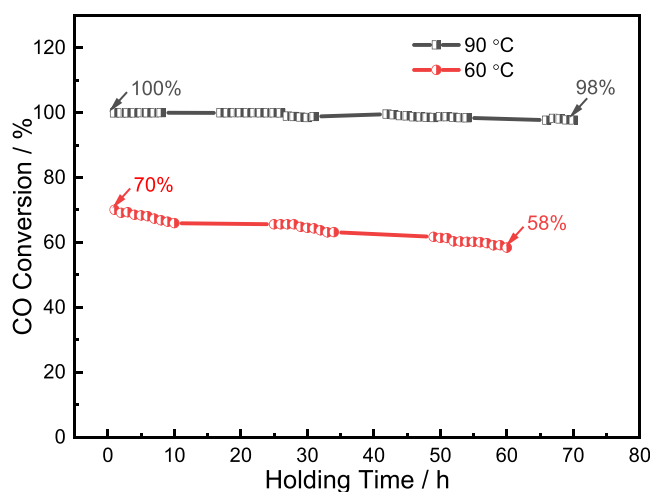

Figure 8. Long-term stability of $(Pd_{0.15}-Au_{0.15})/CeO_2$ catalyst.

composition, which can guarantee rich diffusion paths and reactive sites for catalytic process. Highly concentrated Ce^{3+}, Au^0, Au^{3+}, and Pd^0 as well as Pd^{2+} species exist in $(Au_{0.15}-Pd_{0.15})/CeO_2$ catalyst. The existence of noble metal active phases is conducive to adsorption of CO onto the surface of the catalyst, and the highly concentrated Ce^{3+} can provide more oxygen vacancies, which is beneficial for generation of more active oxygen atoms. The interaction between Au and Pd/PdO nanoparticles as well as the nanoscale interface between Au (Pd/PdO) and CeO_2 can promote the movement of electrons at the interface. The electrons can not only quickly activate the CO gas adsorbed by noble metals but also accelerate the dissociation of generated CO_2 on the catalyst surface, thus ultimately making the reaction rate increase.

■ CONCLUSIONS

In summary, the nanorod-shaped $(Au-Pd)/CeO_2$ catalysts are fabricated through a combined dealloying and calcination method. The $(Au-Pd)/CeO_2$ catalysts prepared from the Al−Ce−Au−Pd precursor alloys possess an interspersed nanorod structure with nanopores distributed among them. By rationally adjusting the Pd/Au ratio, the achieved $(Pd_{0.15}-Au_{0.15})/CeO_2$ achieves a unique nanorod structure and rich active sites, which contribute to exceptional catalytic activity with T_{50} and T_{99} as low as 50 and 85 °C, respectively. This work provides a new strategy for preparing high performance catalysts by combing

earth metal oxides with noble bimetal materials through a simple and industrial method.

EXPERIMENTAL SECTION

Material Preparation. The $Al_{90}Ce_{10}$, $Al_{91.7}Ce_8Pd_{0.3}$, $Al_{91.7}Ce_8Au_{0.3}$, $Al_{91.7}Ce_8Au_{0.05}Pd_{0.25}$, $Al_{91.7}Ce_8Au_{0.1}Pd_{0.2}$, and $Al_{91.7}Ce_8Au_{0.15}Pd_{0.15}$ alloy ingots were achieved from pure Al, Ce, Au, and Pd through an arc-melting method under a high-purity Ar atmosphere. The obtained alloy ingots were then remelted and solidified into an alloy ribbon 4−6 mm wide and 40−70 μm thick. The quenched alloy ribbons were dealloyed in 20 wt % NaOH aqueous solution at room temperature for 2 h until no obvious bubbles were generated and most of the Al was removed. Ultimately, after a cleaning and drying procedure, the dealloyed samples were calcined at 400−600 °C for 2 h under pure O_2 environment.

Materials Characterization. The phase composition was explored by X-ray diffractometry (XRD, Bruker D8 Advance). Surface morphologies were tested by field emission scanning electron microscopy (FESEM, JEOL, JSM-7000F) and high-resolution transmission electron microscopy (HRTEM, JEOL, JEM-2100). The scanning transmission electron microscopy (STEM, FEI-200) equipped with an Oxford Instruments EDS spectrometer was utilized to conduct EDS analysis and mapping. X-ray photoelectron spectroscopy (XPS) was tested on ESCALAB Xi+ to confirm the element composition and valence state. Nitrogen sorption was tested on a Micromeritics ASAP 2020 at 77 K, and the Barrett−Joyner−Halenda algorithm was adopted to evaluate pore size and pore volume. Raman spectra were collected through an HR 800 fully automatic laser Raman spectrometer. Inductively coupled plasma (ICP) measurement was performed on Prodigy7. The emission lines of Ce 413.765 nm, Pd 342.124 nm, and Au 242.795 nm were acquired for the analysis of the catalysts.

Catalytic Evaluations. The catalytic activity was detected in a tubular reactor at atmospheric pressure. 100 mg of sample was placed into the reactor and fixed with quartz wool. The mixed reaction gas consisting of 1% CO, 10% O_2, and 89% N_2 (volume fraction) was entered into the test system at a flow rate of 100 mL min^{-1} (space velocity 60,000 h^{-1}). The inflowed and outflowed gases were collected by an Anglit 7890B gas chromatograph equipped with a hydrogen flame detector (FID). The CO conversion was determined by

$$CO\ conversion = \frac{C_{in} - C_{out}}{C_{in}} \times 100 \tag{1}$$

where C_{in} and C_{out} represent the concentration of the CO inlet and outlet of the reactor, respectively.

ASSOCIATED CONTENT

Ⓢ Supporting Information

The Supporting Information is available free of charge at https://pubs.acs.org/doi/10.1021/acsomega.2c07191.

Figures of XRD, STEM, and EDS characterization, Raman spectra, as well as catalytic performance (PDF)

AUTHOR INFORMATION

Corresponding Author

Zongcheng Miao − *Key Laboratory of Organic Polymer Photoelectric Materials, School of Sciences, Xi'an Key Laboratory of Advanced Photo-Electronics Materials and Energy Conversion Device, Xijing University, Xi'an, Shaanxi 710123, P. R. China; Present Address: School of Artificial Intelligence, Optics and Electronics (iOPEN), Northwestern Polytechnical University, Xi'an, Shaanxi 710072, P.R. China.;* ⓞ orcid.org/0000-0002-9781-3918; Email: miaozongcheng@nwpu.edu.cn

Authors

Haiyang Wang − *Key Laboratory of Organic Polymer Photoelectric Materials, School of Sciences, Xi'an Key Laboratory of Advanced Photo-Electronics Materials and Energy Conversion Device, Xijing University, Xi'an, Shaanxi 710123, P. R. China*

Dongxia Zhang − *Key Laboratory of Organic Polymer Photoelectric Materials, School of Sciences, Xi'an Key Laboratory of Advanced Photo-Electronics Materials and Energy Conversion Device, Xijing University, Xi'an, Shaanxi 710123, P. R. China*

Ruiyin Zhang − *Key Laboratory of Organic Polymer Photoelectric Materials, School of Sciences, Xi'an Key Laboratory of Advanced Photo-Electronics Materials and Energy Conversion Device, Xijing University, Xi'an, Shaanxi 710123, P. R. China*

Hao Ma − *Key Laboratory of Organic Polymer Photoelectric Materials, School of Sciences, Xi'an Key Laboratory of Advanced Photo-Electronics Materials and Energy Conversion Device, Xijing University, Xi'an, Shaanxi 710123, P. R. China*

Huimin Zhang − *Key Laboratory of Organic Polymer Photoelectric Materials, School of Sciences, Xi'an Key Laboratory of Advanced Photo-Electronics Materials and Energy Conversion Device, Xijing University, Xi'an, Shaanxi 710123, P. R. China*

Ruijuan Yao − *Key Laboratory of Organic Polymer Photoelectric Materials, School of Sciences, Xi'an Key Laboratory of Advanced Photo-Electronics Materials and Energy Conversion Device, Xijing University, Xi'an, Shaanxi 710123, P. R. China*

Miaomiao Liang − *Key Laboratory of Organic Polymer Photoelectric Materials, School of Sciences, Xi'an Key Laboratory of Advanced Photo-Electronics Materials and Energy Conversion Device, Xijing University, Xi'an, Shaanxi 710123, P. R. China; Present Address: School of Materials Science and Engineering, Xi'an Polytechnic University, Xi'an, Shaanxi 710048, P.R. China;* ⓞ orcid.org/0000-0001-9033-2364

Yuzhen Zhao − *Key Laboratory of Organic Polymer Photoelectric Materials, School of Sciences, Xi'an Key Laboratory of Advanced Photo-Electronics Materials and Energy Conversion Device, Xijing University, Xi'an, Shaanxi 710123, P. R. China*

Complete contact information is available at:
https://pubs.acs.org/10.1021/acsomega.2c07191

Author Contributions

‡H.W. and D.Z. contributed equally to this work.

Notes

The authors declare no competing financial interest.

ACKNOWLEDGMENTS

◼ REFERENCES

(1) Wang, L. N.; Li, X. N.; He, S. G. Recent research progress in the study of catalytic CO oxidation by gas phase atomic clusters. *Sci. China Mater.* **2020**, *63*, 892−902.

(2) Akimoto, H. Global air quality and pollution. *Science* **2003**, *302*, 1716−1719.

(3) Lei, L.; Huang, D.; Cheng, M.; Deng, R.; Chen, S.; Chen, Y.; Wang, W. Defects engineering of bimetallic Ni-based catalysts for electrochemical energy conversion. *Coord. Chem. Rev.* **2020**, *418*, 213372.

(4) Jiang, B.; Li, L.; Bian, Z.; Li, Z.; Sun, Y.; Sun, Z.; Tang, D.; Kawi, S.; Dou, B.; Goula, M. A. Chemical looping glycerol reforming for hydrogen production by Ni@ZrO₂ nanocomposite oxygen carriers. *Int. J. Hydrogen Energy* **2018**, *43*, 13200−13211.

(5) Zhang, L.; Filot, I. A. W.; Su, Y. Q.; Liu, J. X.; Hensen, E. J. M. Understanding the impact of defects on catalytic CO oxidation of LaFeO₃-supported Rh, Pd, and Pt single-atom catalysts. *J. Phys. Chem. C* **2019**, *123*, 7290−7298.

(6) Van Spronsen, M. A.; Frenken, J. W. M.; Groot, I. M. N. Surface science under reaction conditions: CO oxidation on Pt and Pd model catalysts. *Chem. Soc. Rev.* **2017**, *46*, 4347−4374.

(7) Valechha, D.; Megarajan, S. K.; Al-Fatesh, A.; Jiang, H.; Labhasetwar, N. Low Temperature CO Oxidation Over a Novel Nano-Structured, Mesoporous CeO₂ Supported Au Catalyst. *Catal. Lett.* **2019**, *149*, 127−140.

(8) Gustafson, J.; Balmes, O.; Zhang, C.; Shipilin, M.; Schaefer, A.; Hagman, B.; Merte, L. R.; Martin, N. M.; Carlsson, P. A.; Jankowski, M.; Crumlin, E. J.; Lundgren, E. The role of oxides in catalytic CO oxidation over rhodium and palladium. *ACS Catal.* **2018**, *8*, 4438−4445.

(9) Wang, C.; Yin, H.; Dai, S.; Sun, S. A general approach to noble metal-metal oxide dumbbell nanoparticles and their catalytic application for CO oxidation. *Chem. Mater.* **2010**, *22*, 3277−3282.

(10) Kim, Y. H.; Park, E. D.; Lee, H. C.; Lee, D.; Lee, K. H. Preferential CO oxidation over supported noble metal catalysts. *Catal. Today* **2009**, *146*, 253−259.

(11) Wang, R.; He, H.; Wang, J.; Liu, L.; Dai, H. Shape-regulation: An effective way to control CO oxidation activity over noble metal catalysts. *Catal. Today* **2013**, *201*, 68−78.

(12) Lin, J.; Wang, X.; Zhang, T. Recent progress in CO oxidation over Pt-group-metal catalysts at low temperatures. *Chin. J. Catal.* **2016**, *37*, 1805−1813.

(13) Tsiotsias, A. I.; Ehrhardt, B.; Rudolph, B.; Nodari, L.; Kim, S.; Jung, W.; Charisiou, N. D.; Goula, M. A.; Mascotto, S. Bimetallic Exsolved Heterostructures of Controlled Composition with Tunable Catalytic Properties. *ACS Nano* **2022**, *16*, 8904−8916.

(14) Charisiou, N. D.; Siakavelas, G. I.; Papageridis, K. N.; Motta, D.; Dimitratos, N.; Sebastian, V.; Polychronopoulou, K.; Goula, M. A. The Effect of Noble Metal (M: Ir, Pt, Pd) on M/Ce₂O₃-γ-Al₂O₃ Catalysts for Hydrogen Production via the Steam Reforming of Glycerol. *Catalysts* **2020**, *10*, 790.

(15) Haruta, M.; Tsubota, S.; Kobayashi, T.; Kageyama, H.; Genet, M. J.; Delmon, B. Low-temperature oxidation of CO over gold supported on TiO₂, α-Fe₂O₃, and Co₃O₄. *J. Catal.* **1993**, *144*, 175−192.

(16) Jiang, H. L.; Liu, B.; Akita, T.; Haruta, M.; Sakurai, H.; Xu, Q. Au@ZIF-8: CO oxidation over gold nanoparticles deposited to metal-organic framework. *J. Am. Chem. Soc.* **2009**, *131*, 11302−11303.

(17) Cappellari, P. S.; Soldano, G. J.; Mariscal, M. M. Bimetallic synergy on iridium-gold catalysts for the CO oxidation reaction. *J. Phys. Chem. C* **2022**, *126*, 1742−1750.

(18) Wu, C. H.; Liu, C.; Su, D.; Xin, H. L.; Fang, H. T.; Eren, B.; Zhang, S.; Murray, C. B.; Salmeron, M. B. Author Correction: Bimetallic synergy in cobalt-palladium nanocatalysts for CO oxidation. *Nat. Catal.* **2019**, *2*, 174−174.

(19) Shin, K.; Zhang, L.; An, H.; Ha, H.; Yoo, M.; Lee, H. M.; Henkelman, G.; Kim, H. Y. Interface engineering for a rational design of poison-free bimetallic CO oxidation catalysts. *Nanoscale* **2017**, *9*, 5244−5253.

(20) Pan, Y. T.; Yang, H. Design of bimetallic catalysts and electrocatalysts through the control of reactive environments. *Nano Today* **2020**, *31*, 100832.

(21) Garcia, C.; Truttmann, V.; Lopez, I.; Haunold, T.; Marini, C.; Rameshan, C.; Pittenauer, E.; Kregsamer, P.; Dobrezberger, K.; Stoger-Pollach, M.; Barrabes, N.; Rupprechter, G. Dynamics of Pd dopant atoms inside Au nanoclusters during catalytic CO oxidation. *J. Phys. Chem. C* **2020**, *124*, 23626−23636.

(22) Montini, T.; Melchionna, M.; Monai, M.; Fornasiero, P. Fundamentals and Catalytic Applications of CeO2-Based Materials. *Chem. Rev.* **2016**, *116*, 5987−6041.

(23) Xiao, Y.; Li, H.; Xie, K. Activating Lattice Oxygen at the twisted surface in a mesoporous CeO₂ single crystal for efficient and durable catalytic CO oxidation. *Angew. Chem., Int. Ed. Engl.* **2021**, *60*, 5240−5244.

(24) Abasaeed, A. E.; Al-Fatesh, A. S.; Naeem, M. A.; Ibrahim, A. A.; Fakeeha, A. H. Catalytic performance of CeO₂ and ZrO₂ supported Co catalysts for hydrogen production via dry reforming of methane. *Int. J.Hydrogen Energy* **2015**, *40*, 6818−6826.

(25) Mock, S. A.; Sharp, S. E.; Stoner, T. R.; Radetic, M. J.; Zell, E. T.; Wang, R. CeO₂ nanorods-supported transition metal catalysts for CO oxidation. *J. Colloid Interface Sci.* **2016**, *466*, 261−267.

(26) Huang, X. S.; Sun, H.; Wang, L. C.; Liu, Y.-M.; Fan, K. N.; Cao, Y. Morphology effects of nanoscale ceria on the activity of Au/CeO₂ catalysts for low-temperature CO oxidation. *Appl. Catal. B: Environ.* **2009**, *90*, 224−232.

(27) Hegde, M. S.; Bera, P. Noble metal ion substituted CeO₂ catalysts: Electronic interaction between noble metal ions and CeO₂ lattice. *Catal. Today* **2015**, *253*, 40−50.

(28) Hossain, S. T.; Azeeva, E.; Zhang, K.; Zell, E. T.; Bernard, D. T.; Balaz, S.; Wang, R. A comparative study of CO oxidation over Cu-O-Ce solid solutions and CuO/CeO₂ nanorods catalysts. *Appl. Surf. Sci.* **2018**, *455*, 132−143.

(29) Ye, J.; Cheng, D.; Chen, F.; Zhan, X. Controlled synthesis of sintering-resistant Pd@CeO₂ core-shell nanotube catalysts for CO oxidation. *Ind. Eng. Chem. Res.* **2019**, *58*, 21972−21982.

(30) Qiu, B.; Wang, C.; Zhang, N.; Cai, L.; Xiong, Y.; Chai, Y. CeO₂-induced interfacial Co²⁺ octahedral sites and oxygen vacancies for water oxidation. *ACS Catal.* **2019**, *9*, 6484−6490.

(31) Zhang, X.; Hou, F.; Yang, Y.; Wang, Y.; Liu, N.; Chen, D.; Yang, Y. A facile synthesis for cauliflower like CeO₂ catalysts from Ce-BTC precursor and their catalytic performance for CO oxidation. *Appl. Surf. Sci.* **2017**, *423*, 771−779.

(32) Maurer, F.; Beck, A.; Jelic, J.; Wang, W.; Mangold, S.; Stehle, M.; Wang, D.; Dolcet, P.; Gänzler, A. M.; Kübel, C.; Studt, F.; Casapu, M.; Grunwaldt, J.-D. Surface noble metal concentration on ceria as a key descriptor for efficient catalytic CO oxidation. *ACS Catal.* **2022**, *12*, 2473−2486.

(33) Muravev, V.; Spezzati, G.; Su, Y. Q.; Parastaev, A.; Chiang, F.-K.; Longo, A.; Escudero, C.; Kosinov, N.; Hensen, E. J. M. Interface dynamics of Pd-CeO₂ single-atom catalysts during CO oxidation. *Nat. Catal.* **2021**, *4*, 469−478.

(34) Sun, Y.; Liu, W.; Tian, M.; Wang, L.; Wang, Z. A Rational Design of the Sintering-Resistant Au-CeO(2) nanoparticles catalysts for CO oxidation: the influence of H(2) pretreatments. *Materials* **2018**, *11*, 1952.

(35) Smal, E.; Bespalko, Y.; Arapova, M.; Fedorova, V.; Valeev, K.; Eremeev, N.; Sadovskaya, E.; Krieger, T.; Glazneva, T.; Sadykov, V.;

Simonov, M. Carbon Formation during Methane Dry Reforming over Ni-Containing Ceria-Zirconia Catalysts. *Nanomaterials-Basel* **2022**, *12*, 3676.

(36) Sasirekha, N.; Sangeetha, P.; Chen, Y. W. Bimetallic Au-Ag/CeO$_2$ catalysts for preferential oxidation of CO in hydrogen-rich stream: effect of calcination temperature. *J. Phys. Chem. C* **2014**, *118*, 15226−15233.

(37) McCue, I.; Benn, E.; Gaskey, B.; Erlebacher, J. Dealloying and dealloyed materials. *Annu. Rev. Mater. Res.* **2016**, *46*, 263−286.

(38) Zhang, J.; Chan, L. C.; Gao, T.; Wang, Q.; Zeng, S.; Bian, H.; Lee, C.; Xu, Z.; Li, Y. Y.; Lu, J. Bulk monolithic electrodes enabled by surface mechanical attrition treatment-facilitated dealloying. *J. Mater. Chem. A* **2016**, *4*, 15057−15063.

(39) Sang, Q.; Hao, S.; Han, J.; Ding, Y. Dealloyed nanoporous materials for electrochemical energy conversion and storage. *EnergyChem.* **2022**, *4*, 100069.

(40) Imhanria, S.; Deng, X.; Tan, T.; Deng, J.; Xu, L.; Wang, W. Phosphating a Pd-rich 'dealloyed PdCo$_3$ nanoparticles': An effective electrocatalyst for glycerol oxidation reaction. *J. Alloys Compd.* **2021**, *868*, 159058.

(41) Luo, L.-M.; Zhan, W.; Zhang, R.-H.; Hu, Q.-Y.; Guo, Y.-F.; Zhou, X.-W. Enhanced catalytic activity and stability of CoAuPd nanocatalysts by combining methods of heat treatment and dealloying. *J. Catal.* **2020**, *381*, 316−328.

(42) Zhang, X.; Li, K.; Shi, W.; Wei, C.; Song, X.; Yang, S.; Sun, Z. Baize-like CeO$_2$ and NiO/CeO$_2$ nanorod catalysts prepared by dealloying for CO oxidation. *Nanotechnology* **2017**, *28*, 045602.

(43) Xie, Y.; Wu, J.; Jing, G.; Zhang, H.; Zeng, S.; Tian, X.; Zou, X.; Wen, J.; Su, H.; Zhong, C.; Cui, P. Structural origin of high catalytic activity for preferential CO oxidation over CuO/CeO$_2$ nanocatalysts with different shapes. *Appl. Catal., B* **2018**, *239*, 665−676.

(44) Jin, X.; Duan, Y.; Liu, D.; Feng, X.; Li, W.; Zhang, Z.; Zhang, Y. CO Oxidation Catalyzed by Two-Dimensional Co$_3$O$_4$/CeO$_2$ Nanosheets. *ACS Appl.Nano Mater.* **2019**, *2*, 5769−5778.

(45) Zhang, X.; Li, G.; Song, X.; Yang, S.; Sun, Z. Three-dimensional architecture of Ag/CeO$_2$ nanorod composites prepared by dealloying and their electrocatalytic performance. *RSC Adv.* **2017**, *7*, 32442−32451.

(46) Duan, D.; Hao, C.; He, G.; Wen, Y.; Sun, Z. Rh/CeO$_2$ composites prepared by combining dealloying with calcination as an efficient catalyst for CO oxidation and CH4 combustion. *J. Rare Earth.* **2022**, *40*, 636−644.

(47) Charisiou, N. D.; Italiano, C.; Pino, L.; Sebastian, V.; Vita, A.; Goula, M. A. Hydrogen production via steam reforming of glycerol over Rh/γ-Al$_2$O$_3$ catalysts modified with CeO$_2$, MgO or La$_2$O$_3$. *Renewable Energy* **2020**, *162*, 908−925.

(48) Wang, H.; Duan, D.; Ma, C.; Shi, W.; Liang, M.; Wang, L.; Song, X.; Gao, L.; Sun, Z. The preparation and catalytic properties of nanoporous Pt/CeO$_2$ composites with nanorod framework structures. *Nanomaterials-Basel* **2019**, *9*, 683.

(49) Wang, H.; Mao, Q.; Yu, H.; Wang, S.; Xu, Y.; Li, X.; Wang, Z.; Wang, L. Enhanced electrocatalytic performance of mesoporous Au-Rh bimetallic films for ammonia synthesis. *Chemical Engineering Journal* **2021**, *418*, 129493.

(50) Lv, Y.; Han, Z.; Jia, R.; Shi, L.; Yuan, S. Porous interface for fast charging silicon anode. *Battery Energy* **2022**, *1*, 20220009.

(51) Kasim, S. O.; Al-Fatesh, A. S.; Ibrahim, A. A.; Kumar, R.; Abasaeed, A. E.; Fakeeha, A. H. Impact of Ce-Loading on Ni-catalyst supported over La$_2$O$_3$+ZrO$_2$ in methane reforming with CO$_2$. *Int. J. Hydrogen Energy* **2020**, *45*, 33343−33351.

(52) Li, X.; Feng, J.; Perdjon, M.; Oh, R.; Zhao, W.; Huang, X.; Liu, S. Investigations of supported Au-Pd nanoparticles on synthesized CeO$_2$ with different morphologies and application in solvent-free benzyl alcohol oxidation. *Appl. Surf. Sci.* **2020**, *505*.144473

(53) Jiang, J.; Lei, J.; Hu, Y.; Bi, W.; Xu, N.; Li, Y.; Chen, X.; Jiang, H.; Li, C. Electron transfer effect from Au to Pt in Au-Pt/TiO$_2$ towards efficient catalytic activity in CO oxidation at low temperature. *Appl. Surf. Sci.* **2020**, *521*.146447

(54) Deng, Y.; Tian, P.; Liu, S.; He, H.; Wang, Y.; Ouyang, L.; Yuan, S. Enhanced catalytic performance of atomically dispersed Pd on Pr-doped CeO$_2$ nanorod in CO oxidation. *J. Hazard Mater.* **2022**, *426*, 127793.

(55) Yan, Y.; Li, H.; Lu, Z.; Wang, X.; Zhang, R.; Feng, G. Effects of reduction temperature and content of Pd loading on the performance Pd/CeO$_2$ catalyst for CO oxidation. *Chin. Chem. Lett.* **2019**, *30*, 1153−1156.

(56) Han, B.; Li, H.; Li, L.; Wang, Y.; Zhang, Y.; Li, G. Kinetic control of CeO$_2$ nanoparticles for catalytic CO oxidation. *J. Mater. Res.* **2019**, *34*, 2201−2208.